BNL-228527-2025-JAAM

Biogeochemical Controls on Wood Degradation as a Source of Bioavailable Carbon in Denitrifying Bioreactors

Y. Sang, R. Tappero

To be published in "Environmental Science & Technology"

June 2025

Photon Sciences

Brookhaven National Laboratory

U.S. Department of Energy

USDOE Office of Science (SC), Basic Energy Sciences (BES). Scientific User Facilities (SUF)

DISCLAIMER

Biogeochemical Controls on Wood Degradation as a Source of Bioavailable Carbon in Denitrifying Bioreactors

Yi Sang[1], Iva Petrovic[1], Lily Elaine DuPlooy[1], Zihao Zhang[1], Ryan Tappero[2], Mingyuan Ge[2], Lin Yang[2], and Matthew C. Reid[1*]

[1]School of Civil and Environmental Engineering, Cornell University, Ithaca NY 14853, USA

[2]National Synchrotron Light Source II, Brookhaven National Laboratory, Upton, NY 11973, USA

*Corresponding author: mcr239@cornell.edu

Keywords: Woodchip bioreactor, lignocellulose, denitrification, wood degradation, iron, manganese, oxidative decomposition, X-ray scattering, XANES

Abstract

Woodchip bioreactors (WBRs) are important tools for the removal of nitrate in agricultural drainage, but their effectiveness is often limited by the slow degradation of lignocellulosic wood residues into bioavailable forms of carbon that fuel denitrifying microorganisms. Here, we examine biogeochemical factors regulating wood degradation in saturated woodchip beds, with a focus on the effects of dissolved oxygen (DO), iron (Fe), and manganese (Mn) in generating oxidative activity that can enhance wood decomposition. Woodchips from a 10-yr old WBR were characterized with bulk techniques and a novel combination of μX-ray scattering, μXRF, and μXANES to visualize the depletion of crystalline cellulose as a proxy for wood degradation. Woodchips from upstream portions of the reactor exhibited the greatest degradation, probably due to greater DO exposure, and degradation was localized to a 100 to 200 μm thick surface layer that was also associated with higher concentrations of Fe and Mn. Greater degradation was associated with faster nitrate removal. μXANES analysis of Fe and Mn in the surface layer indicated the presence of a microenvironment where oxygenation reactions of Fe(II) and Mn(II) could contribute to the formation of reactive oxidants involved in the degradation of lignocellulose. Our results provide new insight into biogeochemical properties that influence wood decomposition in WBRs at both micro- and macro-scales, and how these wood degradation processes are coupled with denitrification.

Synopsis

Degradation of wood biomass into bioavailable carbon is a bottleneck that limits the effectiveness of denitrifying bioreactors treating agricultural drainage. This study describes spatial relationships between wood degradation and biogeochemical properties of decomposing wood at both the micro- and macro-scale, and proposes a role for redox reactions of iron and manganese as a potential source of reactive oxidants that can enhance the oxidative degradation of wood and increase the supply of bioavailable carbon for denitrifying microbes.

1. Introduction

Woodchips and other lignocellulosic residues are widely used as renewable and widely-available electron donor sources for heterotrophic denitrifying microorganisms in nature-based systems including horizontal levees[1], stormwater biofilters[2], managed aquifer recharge basins[3], and woodchip bioreactors (WBRs) treating agricultural drainage[4-6]. While woodchips can initially release significant amounts of labile dissolved organic carbon (DOC) in the early stages of decomposition, DOC release slows considerably when woodchips are aged under saturated conditions[7], causing denitrification in many WBRs to become carbon-limited[5]. This has been attributed to the stability of lignin under anoxic conditions[8], with the persistence of lignin protecting underlying cellulose and hemicellulose (holocellulose) biopolymers from biodegradation[9]. Biogeochemical factors controlling holocellulose bioavailability in saturated conditions have important implications for the long-term effectiveness of woodchip and other lignocellulose-based denitrifying systems, but are not well understood.

There is significant spatial variability in woodchip media properties after weathering under *in situ* bioreactor conditions. Woodchips excavated from the influent end of bioreactors are more degraded than those near the effluent after 2 to 4 yr of weathering, as measured by a lower C/N ratio and a higher lignocellulose index (LCI), indicating a depletion of cellulose relative to lignin[10-11]. Greater degradation was correlated with faster nitrate (NO_3^-) removal rates[10], underscoring the importance of wood decomposition as a driver of denitrification. While these observations may be related to higher dissolved oxygen (DO) concentrations near influents[11] and the ability of

oxygen (O_2) to stimulate extracellular fungal ligninolytic enzymes[12-14], other studies have found no relationship between DO levels and wood decay[10]. A recent analysis of WBR subsidence in field-scale WBRs, a result of wood mass loss over time, also suggested that O_2 exposure alone is insufficient to explain variations in subsidence[15]. Woodchips also entrain inorganic material when storm events transport suspended soil particles into WBRs[10, 16]. Woodchips recovered from a field bioreactor were enriched in iron (Fe), aluminum (Al), and magnesium (Mg) compared to "fresh" woodchips sourced from lumber yards[17], and an ash content as high as 22% has been observed in woodchips excavated from a 2 yr old bioreactor[10]. Notably, the ash content was highest in woodchips where C/N ratios and LCI indicated the most advanced degradation[10].

The presence of minerals in woodchip media may have implications for wood degradation and carbon bioavailability for denitrifying microorganisms. Mineral protection theories, which emerged from studies of organic matter dynamics in soils, suggest that Fe- and manganese (Mn) oxide minerals could decrease the bioavailability of wood-derived organic carbon through processes including adsorption or physical trapping[18-24]. However, emerging research has challenged mineral protection paradigms and highlighted the roles of Mn and Fe in promoting the oxidative decomposition of lignocellulosic biomolecules[25]. These oxidative processes include the oxidation of Mn(II) to Mn(III) by fungal manganese peroxidase (MnP) enzymes followed by Mn(III)-driven oxidation of phenolic moieties in lignin[26]; and the production of hydroxyl radicals (•OH) and other reactive oxygen species via Fe(II) oxidation at oxic-anoxic interfaces[27-29]. These Mn- and Fe-dependent mechanisms are utilized by fungal white and brown rot phenotypes, respectively, in the degradation of woody biomass[30-31]. There has been substantial biogeochemical research into organo-mineral interactions as a control of carbon stability in soils[25, 27, 32], but the

impacts of these processes on wood degradation and carbon availability in saturated denitrifying woodchip beds is unknown.

We hypothesized that higher concentrations of Fe and Mn in the woodchip matrix enhance the oxidative decomposition of wood biomass, particularly under redox-fluctuating conditions or at redox interfaces, leading to more bioavailable carbon and faster NO_3^- removal by woodchip biofilms. Potential Fe- and Mn-driven effects on wood decomposition have implications for the long-term effectiveness of wood as an electron donor source in WBRs, as well as for understanding woody biomass decay with relevance to the global carbon cycle[33-35]. There has been little focus on the role of metals in biogeochemical pathways for wood degradation in denitrifying bioreactors, despite the fact that large amounts of inorganic sediment can be transported into woodchip beds[10, 16, 36]. We used a novel combination of synchrotron-based μX-ray scattering, μXRF imaging, and μXANES spectroscopy to probe micro-scale relationships between cellulose crystallinity, a quantitative indicator of lignocellulose decay[37], and metal speciation in wood in a field-scale WBR. This micro-scale analysis of wood decomposition informs a macro-scale understanding of WBR denitrification function.

2. Materials and Methods

Field Bioreactor and Woodchip Sample Collection. Paired woodchip bioreactors were installed in Freeville, NY, in 2012 to treat tile drainage containing roughly 8 mg/L NO_3^--N from 8 hectares of vegetable fields. The dimensions of each reactor is 6.1 m long × 3.1 m wide × 0.69 m thick, with a 0.35 m soil cap. In October 2022 we collected primarily ash (*Fraxinus* sp.) woodchips that

had been weathering for ten years[38-40]. Woodchips were excavated from upstream (0.6 m from reactor inlet), midstream (3 m from reactor inlet), and downstream (5.5 m from reactor inlet) locations at three different depths for each longitudinal position (0-5 cm below the bioreactor surface; 30-35 cm below the bioreactor surface; and 60-65 cm below the bioreactor surface), for a total of 9 sample locations (Fig. S1). Sample locations and labels are summarized in Table 1. Woodchips were frozen at -20°C within 3 hr of being collected until later characterization. The bioreactor has a V-notch weir in the outlet control structure that maintains water levels at a depth > 49 cm in the woodchip bed. A pressure transducer (Campbell Scientific CS451) mounted in the outlet structure was used to monitor water levels and determine bioreactor discharge. In the summer of 2023, DO concentrations in the woodchip bed 0.1 and 6 m from the bioreactor inlet were monitored using DO sensors (Campbell scientific CS511-L)[41] to provide representative data on DO concentrations in upstream and downstream portions of the reactor.

Bulk Woodchip Properties. Total Mn and Fe concentrations on woodchip surfaces were determined by lightly rinsing 2.8 ± 0.35 g (dry weight) of woodchips with ~500 ml of tap water and then extracting with 6 M HCl for 4 h in a 50 ml polypropylene centrifuge tube on a tube rotator. Extracts were filtered through a 0.2 μm PES filter and analyzed for metal concentrations via ICP-MS. C/N ratios were determined using an NC2500 elemental analyzer (Carlo Erba, Italy). The protein concentration on woodchip surfaces, a measure of microbial biomass, was determined using the Pierce BCA protein assay (see SI for additional details). Extractable DOC was quantified using pyrophosphate (PP)[34, 42] and potassium chloride (KCl) extractions of woodchips, with the difference between PP- and KCl-extractable carbon indicating DOC chelated with metals[34, 42-43] (see SI for details). All woodchip properties were measured in triplicate samples from each

location. Three wood specimens collected from the field woodchip bioreactor were also characterized using SEM (Zeiss LEO 1550 FESEM).

Woodchip Batch Incubations. Woodchips were stored at -20°C for approximately one year after field collection, then thawed at room temperature for one day. They were gently rinsed in tap water until there was no visual evidence for additional mineral material being rinsed away, and pre-incubated in a synthetic bioreactor media (1 mM $NaNO_3$, 3mM KCl, 0.2 mM Na_2SO_4, 1 mM $NaHCO_3$, and 0.2 mM NaH_2PO_4, adjusted to pH 7.2 ± 0.1) for two weeks at room temperature (22°C). Samples were then dried in air for two days before being placed in triplicate batch reactors for each of the nine locations. 17.5 ± 0.2 g of woodchips (dry weight) were added to 90 ml of the synthetic media in 120-ml glass bottles sealed with gas-tight bromobutyl stoppers, leaving approximately 5-10 mL of headspace. Bottles were wrapped in foil to avoid light exposure and incubated at room temperature for two weeks without shaking. Water samples were collected six times over eight days and filtered through 0.2 μm PES filters for analysis of NO_3^-, DOC released from wood, and specific ultraviolet absorbance at 254 nm ($SUVA_{254}$), a measure of carbon aromaticity[44].

Oxidative activities of woodchip specimens at the termination of batch incubations were measured with the L-3,4 dihydroxyphenylalanine (L-DOPA) probe method, a widely-used assay for enzymatic and nonenzymatic oxidation of lignin-like phenolic compounds[27-28, 45-46]. Woodchips were suspended in a mixture of 7.5 ml of 12.5 mM L-DOPA and 7.5ml of 50 mM sodium acetate buffer (pH 4.7) and shaken on an orbital shaker under oxic conditions for 2.5 hr, and L-DOPA

oxidation was measured using UV-Vis spectroscopy. Additional details are available in SI. While the L-DOPA technique does not distinguish between specific oxidative mechanisms, L-DOPA oxidative activities have been linked to phenol oxidases (without added H_2O_2) and peroxidases (with added H_2O_2)[45, 47-48], as well as reactive oxygen species produced by Fenton reactions driven by Fe(II) oxidation[27]. Control experiments were performed with L-DOPA and H_2O_2 without woodchips to confirm that measured oxidative activities were wood-driven. Production of hydroxyl radicals and other reactive oxidants from Fe(II) oxidation is highly pH-dependent[49-50], and we acknowledge that the pH of the L-DOPA assay (4.7) is lower than the pH of the bulk liquid in the bioreactor. However, the pH in the surface layers of decomposing wood where we propose that Fe(II) oxidation is occurring is most likely lower than the bulk solution pH[51-53]. The oxidative activity was then calculated using a molar extinction coefficient of 1832 M^{-1} cm^{-1}, and the results were reported in μmol of oxidized L-DOPA per g of woodchip (dry weight)[54].

Wet Chemical and Optical Analyses. Filtered water samples for elemental analysis were preserved in 2% trace metal grade nitric acid and analyzed with an Agilent 7800 ICP-MS with an He collision cell. QA/QC was routinely assessed with check standards, blanks, and repeat measurements of samples. DOC was measured using a Shimadzu TOC analyzer (NPOC method). Optical measurements for the L-DOPA assay and determination of $SUVA_{254}$ were performed with a Shimadzu UV-2600i spectrophotometer. NO_3^- was measured using ion chromatography (Dionex ICS-2100).

Synchrotron-based Analysis of Wood Specimens. Frozen woodchip samples collected from the field WBR were thawed, air-dried, and cut into matchstick-sized pieces, with a length of 20-30 mm and a width of 3-4 mm. A specimen of woodchip that had not weathered in the bioreactor was acquired as a non-degraded control. X-ray scattering and fluorescence data were simultaneously collected at the LiX beamline (16-ID)[55] at the National Synchrotron Light Source II (NSLS-II), using a scanning microtomographic imaging approach with a beam size of 5 microns and an X-ray energy of 15.138 keV. The X-ray scattering data were used for structural characterization of crystalline cellulose biopolymers in wood. The tomographic approach was utilized due to difficulties in preparing thin sections of decomposed samples, and to avoid potential errors in X-ray scattering data if sections were not perpendicular to the fibril growth direction[56]. Additional details, including on the tomographic reconstruction of X-ray scattering intensities, are available elsewhere[56-57]. The cellulose crystallinity index (C.I.) describes the relative amount of crystalline material in cellulose, and is interpreted here as a quantitative measure of woodchip degradation[37, 58-60]. The C.I. in each voxel (5µm x 5µm) was determined using:

$$C.I. = \frac{I_{cellulose} - I_{amorphous}}{I_{amorphous}} \qquad (Eqn. 1)$$

where $I_{cellulose}$ and $I_{amorphous}$ are intensities of crystalline and amorphous cellulose, respectively, and are determined by integrating scattering intensities in q-space from 1.56-1.62 and 1.29-1.35 $Å^{-1}$, respectively[56]. Low-intensity voxels were removed to prevent division by zero artifacts[56]. Higher C.I. indicates a greater amount of crystalline cellulose, while lower C.I. indicates a depletion of crystalline cellulose and more advanced degradation. X-ray fluorescence for imaging elemental distributions was collected using a Vortex silicon drift detector with Xspress3 readout electronics, and self-absorption corrections were made using methods described in ref.Ge, et al. [61]

213

214 Separately, transverse and longitudinal thin sections (40 μm) were prepared from freeze-dried
215 woodchip samples from the midstream-middle (M-M) location using a cryo-microtome and stored
216 in heat-sealed mylar bags with O_2 scrubbers until synchrotron analysis to avoid changes in Fe or
217 Mn oxidation states. μXRF elemental maps and K-edge Mn and Fe μXANES spectra were
218 collected at the XFM beamline (4-BM) at NSLS-II with a beam size of 8 μm. Variations in Mn
219 and Fe oxidation states were assessed by comparing the Mn XANES white line energy and the Fe
220 XANES pre-edge centroid energy (Fig. S2)[62-63], respectively. $MnCl_2$, Mn(III) oxide, and
221 birnessite[64] were used as references for Mn(II), Mn(III), and Mn(IV) white line energies, while
222 siderite and ferrihydrite pre-edge centroid energies were used as references for Fe(II) and Fe(III),
223 respectively[63]. Mn(0) (6539 eV) and Fe(0) foils (7112 eV) were used to calibrate the spectra.

224

225 **Results and Discussion**

226

227 **Spatial Variations in Woodchip Properties.** Ten year-old woodchips collected from different
228 locations of the woodchip bed had distinct visual characteristics, with samples from upstream
229 locations having a darker color and a large amount of inorganic material mixed in with the
230 woodchip media (Fig. S3). The upstream portion of the reactor was also characterized by DO
231 concentrations in the bulk water that exceeded 5 mg/L during high-flow periods but then declined
232 to ~2 mg/L during lower-flow periods (Fig. S4), indicating that upstream woodchips were
233 periodically exposed to high DO during their lifetime in the reactor. DO in the downstream portion
234 of the reactor was always < 1 mg/L. We acknowledge that the location of the upstream DO sensor
235 (0.1 m from the reactor inlet) was not perfectly matched to the sampling location of upstream

woodchips (0.6 m from reactor inlet), but the discharge-dependent fluctuations in DO measured at 0.1 m most likely occur, though perhaps to a lesser extent, at the location of the upstream woodchip samples. Research at other bioreactor sites has measured DO concentrations between 6-8 mg/L at a distance of 0.6 m from the reactor inlet[65]. The shallow sampling depth was located above the bioreactor water table throughout the spring and summer of 2023, and would therefore only have been saturated during rare extreme flood events. The middle and deep sampling locations were consistently saturated (Fig. S4).

Table 1. Bulk Woodchip Biogeochemical Properties (dry weight)

†Pyrophosphate-extractable DOC; ‡KCl-extractable DOC

	Upstream			**Midstream**			**Downstream**		
	Shallow U-S	**Middle U -M**	**Deep U -D**	**Shallow M-S**	**Middle M-M**	**Deep M-D**	**Shallow D-S**	**Middle D-M**	**Deep D-D**
Fe (mg/kg)	27.1 ± 10.6	72.7 ± 5.8	102.3 ± 35.2	32.7 ± 3.8	52.8 ± 1.1	40.8 ± 6.2	35.8 ± 6.2	70.8 ± 6.5	38.5 ± 9.3
Mn (mg/kg)	2.5 ± 0.9	12.6 ± 1.4	15.4 ± 3.5	1.04 ± 0.01	3.6 ± 0.2	3.5 ± 1.0	1.4 ± 0.3	2.5 ± 0.3	1.1 ± 0.1
Protein (mg/kg)	579.9 ± 72.7	1131.5 ± 49.6	1096.6 ± 93.8	504.4 ± 28.4	316.8 ± 103.7	315.7 ± 18.3	494.9 ± 39.3	353.3 ± 100.9	321.6 ± 68.1
C/N ratio	244.5 ± 3.6	132.2 ± 36.4	135.2 ± 53.8	228.1 ± 46.6	345.0 ± 33.0	315.1 ± 34.0	279.1 ± 22.3	350.7 ± 44.8	332.4 ± 28.7
DOC_{PP}† (mg /g)	0.53 ± 0.09	0.80 ± 0.03	0.70 ± 0.17	0.49 ± 0.04	0.30 ± 0.03	0.31 ± 0.03	0.36 ± 0.04	0.30 ± 0.03	0.30 ± 0.03
DOC_{KCl}‡ (mg /g)	0.04 ± 0.003	0.05 ± 0.007	0.04 ± 0.009	0.06 ± 0.006	0.03 ± 0.003	0.02 ± 0.003	0.06 ± 0.011	0.03 ± 0.011	0.02 ± 0.001

Woodchips from upstream-deep (U-D) and upstream-middle (U-M) locations had the lowest C/N ratios of 132.2 ± 36.4 and 135.2 ± 53.8, respectively, reflecting a high level of degradation[10] (Table 1). Woodchips from all other locations had C/N ratios > 200. Woodchips from midstream-shallow (M-S) and downstream-shallow (D-S) locations had lower C/N ratios than midstream and

250 downstream samples from saturated depths, suggesting that exposure to air in unsaturated depths
251 may have enhanced decomposition rates.
252
253 The U-D and U-M woodchips were also associated with higher surface Fe and Mn concentrations,
254 consistent with visual evidence of more inorganic material mixed in with upstream woodchips.
255 Protein concentrations were also significantly higher in U-D and U-M woodchips, ranging from
256 1096.6 ± 93.8 to 1131.5 ± 49.6 mg/kg, while protein concentrations in midstream and downstream
257 locations were less than half of those levels, indicating greater biofilm density in upstream
258 saturated zones of the bioreactor. There was a strong inverse relationship between protein
259 concentrations and C/N ratios ($r = -0.96$, $p < 0.05$), highlighting links between greater biomass
260 densities and more degraded wood (Figure S5). Comparison of pyrophosphate (PP) - and KCl-
261 extractable DOC showed that 84%-95% of the potentially leachable DOC was in colloidal form or
262 chelated with metals on woodchip surfaces, and PP-extractable DOC was highest in the U-D and
263 U-M woodchips (Table 1).
264
265 **Batch Incubations.** NO_3^- removal rates were highly variable in anoxic batch incubations, with
266 the U-M, U-D, and M-S woodchips characterized by the fastest rates, removing 65.4, 81.2 and
267 84.0% of NO_3^-, respectively, after 77 hr (Fig. 1A). The upstream samples exhibited a different
268 depth-dependent pattern than the midstream and downstream samples, with faster NO_3^- removal
269 in the saturated upstream locations, while the saturated midstream and downstream samples had
270 the slowest NO_3^- removal. NO_3^- removal was strongly correlated with DOC concentrations
271 released from wood during batch incubations ($r = 0.92$, $p < 0.05$) and surface protein
272 concentrations ($r = 0.72$, $p < 0.05$) (Fig. S5), underscoring important links between wood

degradation, bioavailability of carbon, and enhanced growth of denitrifying microorganisms. It is possible that greater denitrifying activity on upstream woodchips could also be related to differences in the microbial community structure, but analysis of microbial diversity in the woodchips was beyond the scope of the current study. The DOC pool after 8 d of anoxic incubation of upstream samples was more aromatic than that from midstream and downstream locations (Fig. S6C), likely due to greater release of depolymerized lignin residues from the more degraded upstream woodchips[66].

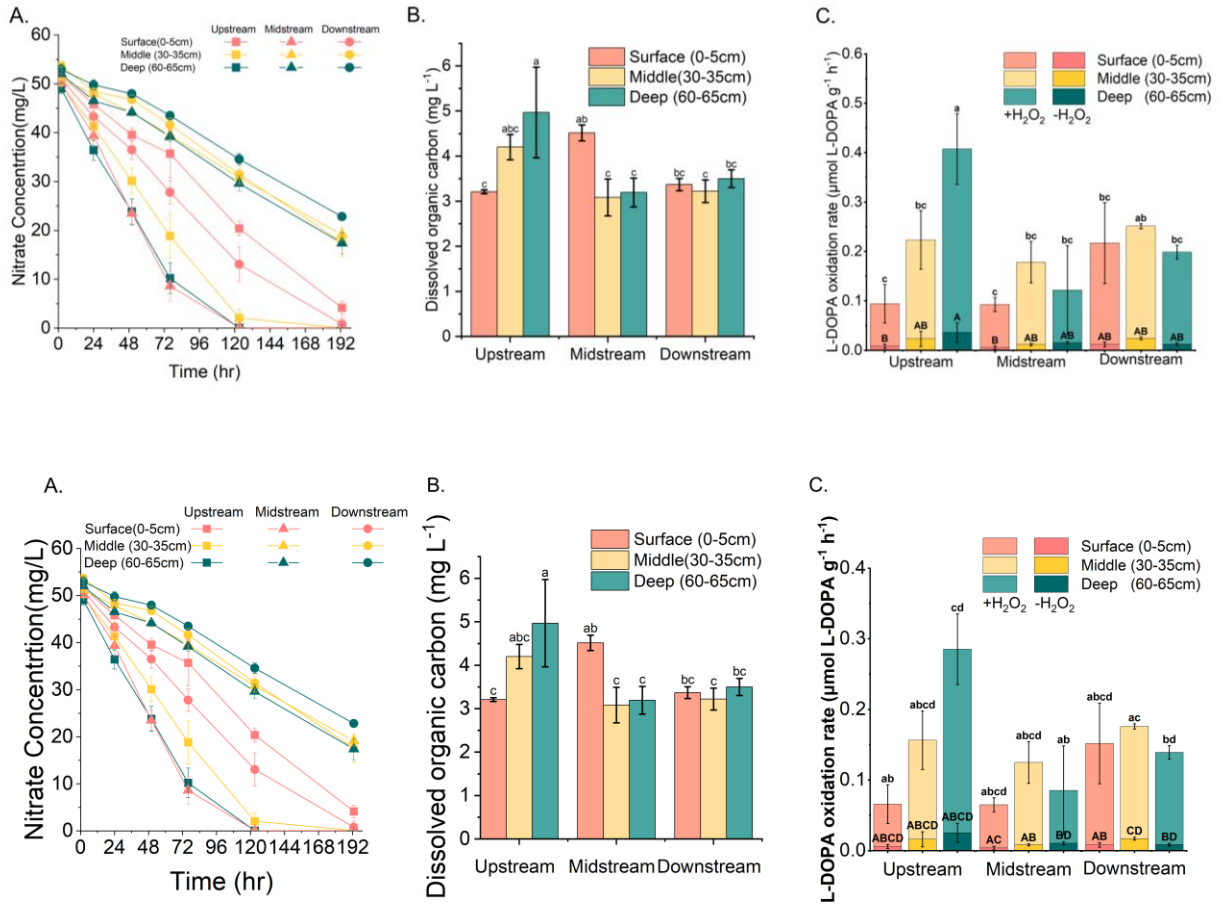

Figure 1. Results of anoxic batch experiments using woodchips from different locations in the 10 year-old bioreactor. **(A)** Nitrate removal; (B) DOC released from woodchips after 8 d of

incubation; (C) Oxidative activities measured using the L-DOPA assay with and without H_2O_2, expressed per dry weight of woodchips, measured after 8 d of anoxic incubation. All measurements were performed in triplicate. Statistically significant differences between samples was determined using one-way ANOVA with Tukey HSD test ($p = 0.05$).

L-DOPA oxidation varied with location, and similar to prior studies in soils[27] was significantly greater in the presence of H_2O_2 (Fig. 1C). L-DOPA oxidation was very strongly associated with Fe ($r = 0.89$, $p < 0.05$) and to a somewhat lesser extent with Mn ($r = 0.72$, $p < 0.05$), with oxidation rates up to 0.41 ± 0.07 μmol L-DOPA g^{-1} woodchip h^{-1} measured in the U-D sample that also had the highest Fe and Mn concentrations (Fig. 1C, S5). Prior observations of correlations between Fe and L-DOPA oxidation in the presence of H_2O_2 have been interpreted as evidence for Fenton reactions[27-28], though it is possible that autocatalytic reactions between L-DOPA and Fe may enhance production of •OH or other reactive oxidants beyond what would occur in natural conditions[27]. However, when all samples were considered there was no relationship between L-DOPA oxidative activity and woodchip C/N ratios, protein, DOC release, or NO_3^- removal (Fig. S5), suggesting that Fe- or Mn-driven oxidative activities did not have a systematic impact on wood decomposition or denitrification function in all portions of the reactor. Because the L-DOPA assay is performed with woodchips in oxic conditions, it represents a "potential" measure of oxidative activity and not a measure of oxidative activity under *in situ* bioreactor conditions, and L-DOPA oxidation may be decoupled from woodchip degradation in midstream and downstream woodchips because they were not routinely exposed to DO. In contrast, for upstream woodchips that were routinely exposed to high DO the L-DOPA assay could provide a more descriptive measure of *in situ* activity. Indeed, when only upstream woodchips were examined there were very

311 strong correlations between L-DOPA oxidative activities and measures of denitrification function
312 (e.g., DOC release, microbial biomass, and NO_3^- removal) while for midstream and downstream
313 woodchips there was either no relationship or there were weak inverse relationships between
314 oxidative activities and denitrification function (Fig. S8).

315

316 **Synchrotron-based structural and elemental characterization of woodchips.** Bulk analysis of
317 woodchip properties suggested that wood degradation rates and pathways depended strongly on
318 location within the bioreactor. We used a novel scanning microtomographic approach[56] to create
319 micro-scale maps of the cellulose crystallinity index (C.I.) and metal concentrations in woodchips
320 to further explore biogeochemical processes regulating wood decay and how they varied spatially
321 within the bioreactor bed (Fig. 2). Virtual sections of intact woodchips showed that lower C.I.
322 values, corresponding to a greater depletion of crystalline cellulose, were concentrated

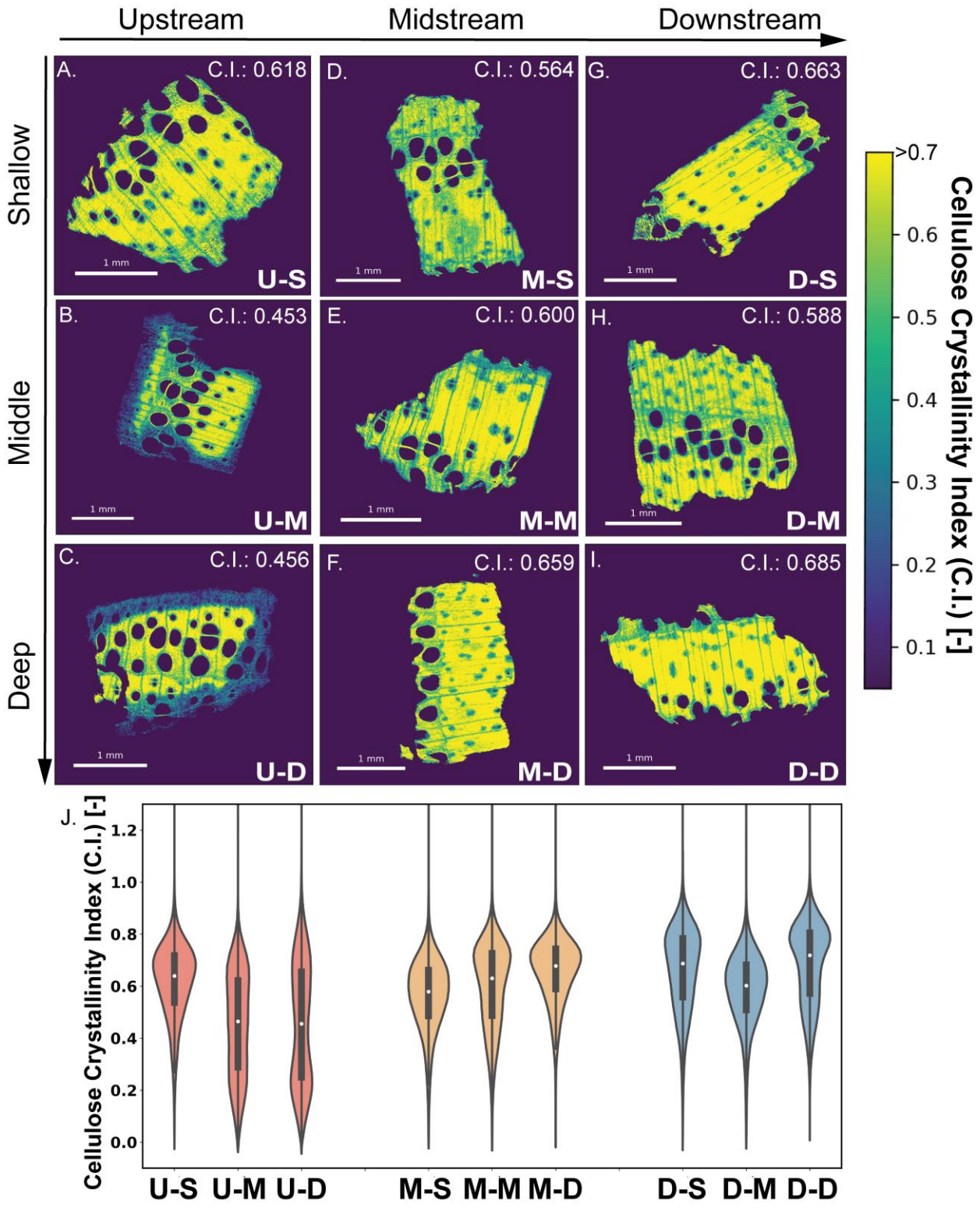

Figure 2. (A-I) Virtual cross-sections obtained with scanning microtomography showing the cellulose crystallinity index (C.I.) of woodchip samples collected from different locations in the

field reactor. Lower C.I. values indicate more degraded wood material. Sampling locations for different woodchip samples are detailed in Fig. S1. The mean C.I. for each sample (calculated as the mean of all wood voxels in each sample) is shown in the upper-right corner of each panel. (J) Violin plots of C.I. Histograms of C.I. distributions are shown in Fig. S12. Pairwise comparisons between samples were performed using the two-sample Kolmogorov-Smirnov test, followed by the Benjamini-Hochberg correction to control the false discovery rate. All corrected p-values were below 0.05, indicating significant differences in the distributions between all samples.

at woodchip surfaces (Fig. 2, S9). Voxels near pores also tended to have a lower C.I. Depletion of crystalline cellulose near surfaces was especially pronounced for the U-M and U-D woodchips, which both had ~250 μm thick bands of highly degraded wood material (C.I. < 0.3) at the surface. Violin plots further showed that the C.I. distributions in U-M and U-D samples were bimodal, with a significant population of near-surface voxels with a lower range of C.I. than is observed in other samples (Fig. 2J). A control woodchip that had not weathered in the bioreactor had high C.I. values throughout the sample with no evidence of surficial degradation (Fig. S10). Even for the most degraded samples including U-M and U-D, there is an intact core of largely undegraded cellulose in the woodchip interior, which may explain how these woodchips continue to supply carbon to sustain fast NO_3^- removal. The mean C.I. shown in Fig. 2 represents analysis of a single sample from each location due to practical limitations with the number of samples that can be analyzed at the synchrotron, though we analyzed a limited number of duplicate samples to demonstrate that the patterns observed in Fig. 2 were generalizable (Fig. S11). In addition, mean C.I. (n=1 samples) and C/N ratios (n=3 samples) from each location were strongly correlated ($r = 0.83$, $p < 0.05$) (Fig. S5), demonstrating agreement between micro- and bulk-scale measurements of wood degradation.

Simultaneous collection of X-ray scattering and fluorescence allowed for the analysis of spatial relationships between cellulose C.I. and metals (Fig. 3). Fe and Mn were both localized on woodchip surfaces, though Fe had greater intensities than Mn, consistent with bulk concentration data (Table 1; Figs. S13, S14). This suggests that Fe and Mn principally originate from exogenous sources, likely soil particles that are transported into reactors and attach to wood surfaces, rather than deriving from wood biomass. In most cases, Fe is located in a thin layer (~50 µm) around the woodchip surface, though the surface of the U-D woodchip was associated with a thicker band of Fe enrichment that overlapped with the band of low C.I shown in Fig. 2C. The upper-right section of the M-M sample was also associated with a thicker layer of Fe enrichment, in a portion of the woodchip that was also associated with a relatively low C.I. (Fig. 2E).

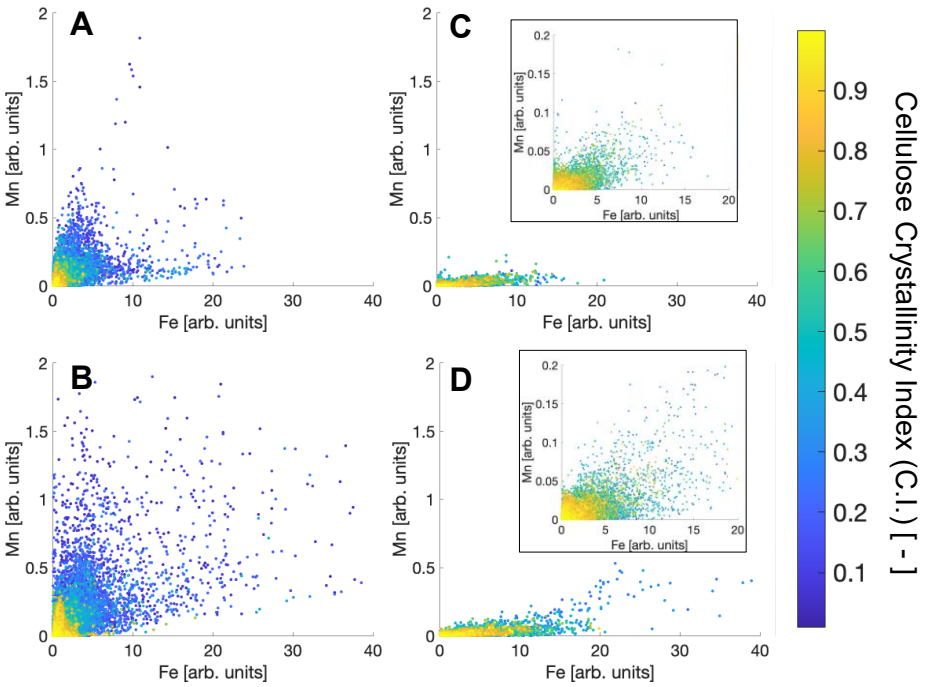

Figure 3. Micro-scale correlations between Fe, Mn, and C.I, obtained using scanning microtomographic analysis of X-ray fluorescence and X-ray scattering data, in **(A)** Upstream-Middle (U-M), **(B)** Upstream-Deep (U-D), **(C)** Downstream-Middle (D-M), and **(D)** Downstream-

Deep (D-D) samples. Each point represents a voxel (5 µm x 5 µm) from images shown in Figure 2. Insets in C and D are zoomed-in to improve visualization at low-Fe and low-Mn levels due to lower metal concentrations in downstream samples. Lower C.I. values indicate more degraded wood material.

We examined micro-scale correlations between Fe, Mn, and C.I. in a subset of samples to assess differences in metal - C.I. relationships between upstream and downstream locations (Fig. 3). In all samples, high-C.I. voxels (defined as C.I. > 0.6) are clustered near the origin where Fe and Mn concentrations are low, while voxels with higher concentrations of Fe and Mn are associated with greater levels of wood degradation (lower C.I.). This was especially clear for the upstream samples which had higher metal concentrations than downstream samples, and where increasing levels of both Fe and Mn were associated with steady decreases in C.I (Fig. 3A, B).

There were a number of differences in Fe-Mn-C.I. correlations between upstream and downstream samples suggesting that Fe and Mn played a more direct role in enhancing wood degradation in upstream locations. For example, in upstream samples essentially all voxels with Fe intensities > 2 (arb. units) had low C.I. (defined as C.I. < 0.3). In contrast, many voxels in downstream samples with the same range of Fe concentrations still had mid- to high-C.I. values (Fig. S15; S16). This suggests that comparable Fe levels had different impacts on upstream vs. downstream woodchips, with Fe intensities > 2 (arb. units) associated with highly degraded wood material in upstream samples while similar Fe levels did not correlate with advanced wood degradation in downstream samples. Mn-C.I. correlations show a similar pattern, with the highest Mn concentrations in each sample strongly associated with low C.I. voxels in upstream but not downstream samples (Fig. S17). Direct comparison between effects of Mn in upstream and downstream samples is

challenging, however, because Mn concentrations were significantly greater in upstream compared to downstream locations. This analysis also shows that in all samples there are voxels with both low metal concentrations and low C.I., indicating that there must be Fe- and Mn-independent pathways for wood degradation in portions of the samples, even while other portions of the samples, particularly in upstream locations, reflect an influence of Fe and/or Mn on enhanced wood degradation.

μXRF and μXANES Analysis of Woodchip Thin Sections. We characterized Fe and Mn at woodchip surfaces using μXRF and μXANES spectroscopy to explore redox dynamics of Fe and Mn that could influence wood decomposition. μXRF imaging of thin-sections confirmed that Fe and Mn were primarily concentrated on or near woodchip surfaces (Fig. 4; S18), though there were examples where metals were also enriched within pores (e.g., Fig. S18 h-j). We also mapped calcium (Ca) concentrations, since Ca hotspots in wood can serve as a biosignature of fungal biomass due to fungal secretion of oxalate and precipitation of Ca oxalate crystals[67], though Ca hotspots could also be related to other Ca-containing minerals. Unlike Fe and Mn, Ca was distributed throughout wood samples in wood rays and vessels due to Ca in biological tissues, though in some cases Ca, Fe, and Mn were co-enriched (e.g., near the wood surface in transect L1, Fig. 4). These and other locations were also enriched in sulfur (bottom row of Fig. S18), and prior μXRF analysis has identified co-enrichment of Ca, Mn, and S as a signature of fungi in decomposing wood[68]. SEM imaging of woodchips collected from the reactor confirmed the presence of fungal mycelia in the wood structure (Fig. S19).

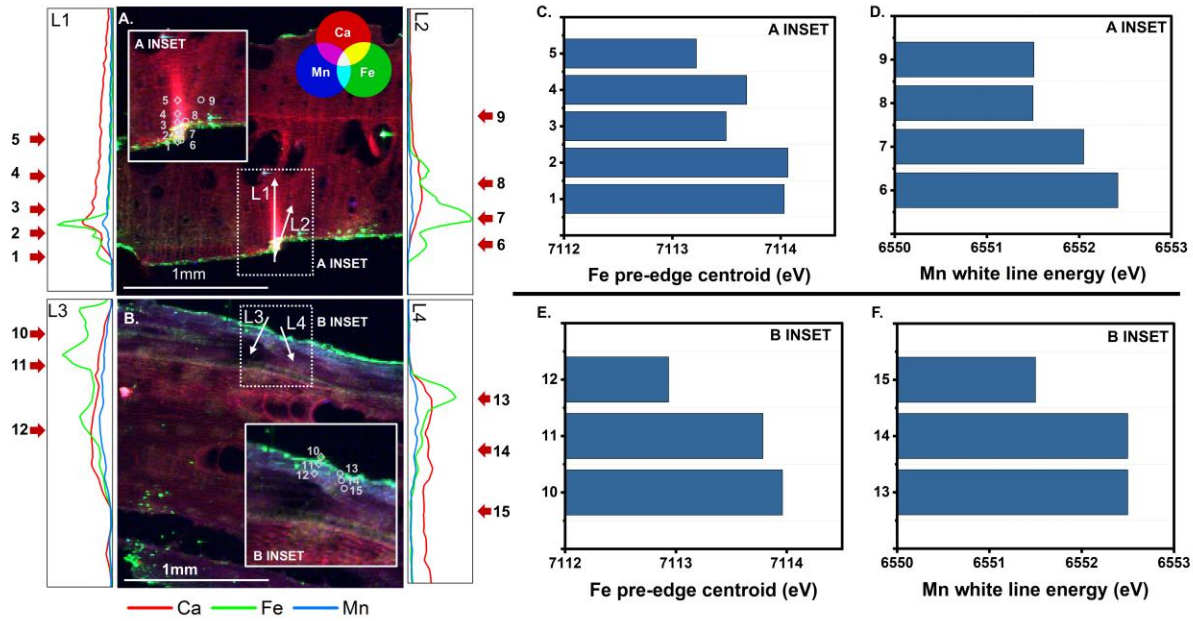

Figure 4. µXRF and µXANES analysis of Fe and Mn distributions and oxidation states in wood thin-sections. Tri-color µXRF images of Fe, Mn, and Ca in (A) transverse and (B) longitudinal thin sections. Insets show zoomed-in images where µXANES spectra were collected along four transects (L1 – L4) moving from the surface to the interior of wood samples. XRF intensities of Fe, Mn, and Ca along transects are shown in boxes to the left and right of panels A and B, with an indication of the location µXANES spectra along the transects. (C, D) Fe pre-edge centroid and Mn white line energies in points of interest 1-9 from transects L1 and L2 in panel A; (E, F) Fe pre-edge centroid and Mn white line energies in points of interest 10-15 from transects L3 and L4 in panel B. Fe and Mn XANES sample and reference spectra are shown in Figure S20.

Fe and Mn µXANES spectra were collected along transects L1 – L4 in Fig. 4 to explore gradients in oxidation state moving from the surface to woodchip interior. For Fe, pre-edge centroid

energies[68] were greatest at the surface and then tended to decrease by 1 to 1.5 eV moving 100 to 200 μm into the woodchip surface layer (Fig. 4C, E), indicating lower Fe oxidation states in the interior and a redox interface within the woodchip surface layer. Pre-edge centroid energies ~7114 eV near the wood surface reflect a mixture of Fe(II) and Fe(III) with a stronger contribution of Fe(III), while a centroid energy ~7113 eV in the wood interior in transect L3 represents primarily Fe(II) (Fig. S20D). Mn followed a similar pattern with relatively higher oxidation states near the surface, though the white line energies between 6551 and 6553 eV all represent Mn oxidation states closer to Mn(II) with a limited contribution from higher oxidation state species (Fig. S20C). Higher oxidation states at surfaces may be related to mineral Fe- and Mn-oxides at woodchip surfaces, while lower oxidation states in the interior surface layer reflect a more reduced environment within the woodchip and its near-surface biofilm. Detailed studies of biofilm communities in decomposing wood have shown that fungal biomass is concentrated inside the wood surface, explaining why reducing microenvironments that depend on labile carbon form within this surface layer[13, 69]. Lower oxidation states of Mn relative to Fe are consistent with Mn(III/IV) oxides being more favorable terminal electron acceptors than Fe(III) oxides and thus being reduced more easily[70]. Prior studies have also reported methanogenic conditions within woodchip biofilms even while the bulk fluid contains NO_3^-, highlighting the deeply reducing conditions that can develop within woodchip biofilms[14]. Lower oxidation states in the interior may also be attributed to Mn(II) and Fe(II) in plant tissues[71-74].

Effect of Woodchip Location on Degradation and Denitrification. Bulk and micro-scale woodchip properties were combined and explored using PCA and K-means clustering (Fig. 5A). The saturated upstream samples (U-D and U-M) clustered separately from the others, along a

451 principal component that explained more than two-thirds of the variation among samples. Higher
452 DO concentrations in the upstream portions of the reactor, particularly during high-flow periods,
453 likely contributed to O_2-dependent pathways for woodchip decay leading to properties of upstream
454 woodchips (including greater biomass and NO_3^- removal) that were distinct from
455 midstream/downstream samples. Fungi are thought to play an important role in wood decay in
456 WBRs[75-76], and SEM images of fungal mycelia along with the co-localization of Ca, S, and Mn in
457 μXRF images support a role for fungal wood decay in the samples characterized here, though our
458 data do not provide information on contributions of white rot vs. brown rot phenotypes. In earlier
459 work, -omics analysis of experimental columns packed with woodchips from the field reactor
460 studied here showed that transient exposure of woodchips to O_2 during column dry-downs
461 stimulated extracellular fungal lignin-degrading enzymes, including MnP, leading to greater
462 carbon availability and denitrification rates after systems returned to anoxia[12, 14]. Fluctuating and
463 occasionally high DO in upstream portions of the field reactor (Fig. S4) likely had a similar impact
464 on enhancing enzymatic degradation of the samples analyzed here, while low DO in downstream

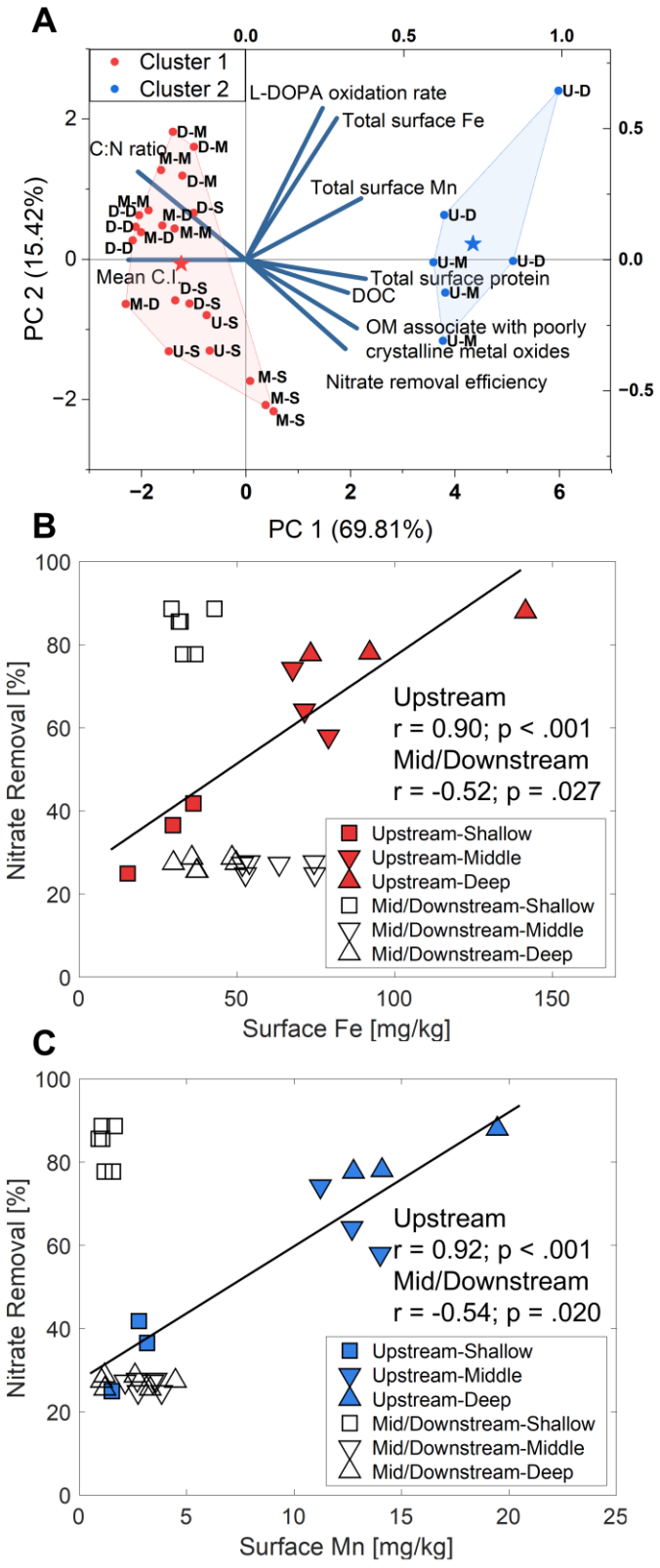
A
Cluster 1
Cluster 2
L-DOPA oxidation rate
Total surface Fe
Total surface Mn
C:N ratio
Mean C.I.
Total surface protein
DOC
OM associate with poorly crystalline metal oxides
Nitrate removal efficiency
PC 1 (69.81%)
PC 2 (15.42%)
B
Nitrate Removal [%]
Surface Fe [mg/kg]
Upstream
r = 0.90; p < .001
Mid/Downstream
r = -0.52; p = .027
Upstream-Shallow
Upstream-Middle
Upstream-Deep
Mid/Downstream-Shallow
Mid/Downstream-Middle
Mid/Downstream-Deep
C
Nitrate Removal [%]
Surface Mn [mg/kg]
Upstream
r = 0.92; p < .001
Mid/Downstream
r = -0.54; p = .020
Upstream-Shallow
Upstream-Middle
Upstream-Deep
Mid/Downstream-Shallow
Mid/Downstream-Middle
Mid/Downstream-Deep

465

Figure 5. Relationships among key woodchip biogeochemical properties. (A) PCA biplot with results shown from each individual replicate of triplicate measurements. Because mean C.I. was determined for just one specimen from each location, the same value of mean C.I. was used for each replicate from that location. The optimal number of clusters in the K-means clustering was determined by the silhouette method and the blue and red stars represent the centroid of the clusters. (B,C) Relationships between woodchip surface Fe or Mn and percentage of NO_3^- removal after 77 h of anoxic batch incubation. Filled symbols show upstream samples and open symbols show midstream and downstream samplers. Lines show a linear model fit to the upstream samples only.

portions limited wood decay. These results are consistent with recent findings in Wang et al.[13], who linked greater fungal biomass near the inlet of a Minnesota WBR to higher DO, and also provided biomolecular evidence for the presence in decomposing woodchips of white rot fungi, some of whom utilize MnP enzymes in the degradation of lignocellulose[77].

Effects of Fe and Mn Redox Dynamics on Wood Degradation. The μXANES analysis of Fe and Mn redox gradients near the wood surface describe an interfacial microenvironment where Fe(II) and Mn(II) species are produced in reducing zones within the woodchip surface layer, creating a microenvironment where they can be microbially oxidized by O_2 or NO_3^- that diffuse into the surface layer[78-80]. Oxygenation of Fe(II) or Mn(II) within this surface layer can generate reactive species involved in depolymerization of lignocellulosic biomolecules[18, 31, 81-82]. For example, Fe(II) oxidation by O_2 can result in the "dark" formation of •OH via Fenton reactions[50, 83], and generated •OH can then depolymerize polysaccharides and/or modify lignin[84]. We caution that while our results with the L-DOPA assay indicate significant phenol oxidative activity with Fe-rich woodchips, we do not have direct evidence for •OH production and would need additional experiments with •OH quenchers to confirm the mechanism. This redox cycling of Fe could be

nonenzymatically mediated by brown rot fungi[85-86], or could also be driven by bacterial reduction of Fe(III) oxides in anaerobic biofilms coupled to abiotic Fe oxidation by dissolved O_2 in the wood surface layer or wood-water interface. H_2O_2 produced by Fe redox reactions or other pathways can then serve as the electron acceptor for MnP enzymes, oxidizing Mn(II) to chelated Mn(III) which can attack phenolic structures in lignin[26, 87].

Differentiating woodchips into upstream vs. midstream/downstream samples clarifies the effects of Fe or Mn on wood decomposition and NO_3^- removal that are distinct from O_2 exposure alone. While there was no relationship between surface metal concentrations and NO_3^- removal when all samples were considered (Fig. 5A), strong correlations between metals and NO_3^- removal in upstream samples are consistent with a role for Fe and/or Mn in stimulating denitrification by enhancing oxidative wood decay and the supply of bioavailable carbon to denitrifiers (Fig. 5B,C). Strong correlations between metals, advanced woodchip degradation (as measured by C/N ratios), and protein concentrations among upstream samples further support this role for metals in portions of the reactor that are exposed to O_2 (Fig. S21,S22). In contrast, metals on midstream/downstream samples had no relationship with protein concentrations (Fig. S21F,H), and exhibited a protective effect on wood decay, with higher metal concentrations associated with less degraded wood (Fig. S21B,D). This protective effect was particularly strong with Fe. Consistent with a possible protective mechanism, metal concentrations on midstream/downstream woodchips were inversely correlated with NO_3^- removal, though the relationships were relatively weak (Fig. 5B, C).

These relationships highlight the potential importance of Fe- or Mn-driven oxidative processes for woodchip degradation and subsequent denitrification, specifically in upstream portions of the reactor. Consistent with these bulk-scale relationships, micro-scale characterization revealed that higher Fe and Mn concentrations in saturated upstream samples led to greater localized wood degradation, while in downstream samples voxels with higher Fe and Mn were not necessarily associated with highly-degraded material (Fig. 3). We propose that metals played an active role in degradation of upstream woodchips, but not midstream/downstream woodchips, because only upstream woodchips were consistently exposed to O_2 that could activate oxygenation reactions of Fe(II) and Mn(II) at wood surfaces that generate reactive oxidants like •OH or Mn(III). This explains why L-DOPA oxidative activities, a measure of oxidative potential under oxic conditions, were only linked to greater DOC release, biomass, and NO_3^- removal in upstream samples but not in midstream/downstream samples where O_2 is depleted (Fig. S7, S8). These results provide new insights into redox dynamics of metals in woodchip surface biofilms, and potential synergies between O_2 exposure and metals in enhancing oxidative wood degradation. While impacts of Fe and Mn redox reactions on organic matter transformation are an area of active research in soil biogeochemistry[25, 27-28, 34], to our knowledge these processes have not been explored in decomposing woody biomass in aquatic systems, and their potential contribution to key WBR properties including wood degradation, denitrification rates, or reactor subsidence have not been examined before this study.

Our analysis provides support for a mineral-enhanced wood degradation process in upstream woodchips that are exposed to fluctuating redox conditions. While most of the potentially leachable DOC from woodchips was associated with metals on woodchip surfaces (Fig. S6), this

535 did not prevent the metal-rich upstream woodchips from releasing the most DOC and fueling the
536 fastest NO_3^- removal during batch incubations (Fig. 1). In contrast, for midstream and downstream
537 woodchips there was some support for a mineral protection process wherein minerals on the wood
538 surface shield wood-derived carbon from microbial activity and slow wood degradation (Fig. S21).
539 We note that metal concentrations on the surfaces of woodchips studied here are relatively low,
540 with Fe concentrations more than ten times lower than those found on woodchips collected from
541 a field reactor in Illinois[17], though this difference may be due to the fact that we rinsed woodchips
542 prior to metal extraction. The effects of metals on wood degradation may be different in the
543 presence of higher metal concentrations.

544

545 An important limitation to our analysis of field-collected woodchip specimens is that causal links
546 between metals and wood degradation are difficult to disentangle from correlation. For example,
547 correlations observed between high metal concentrations and low C.I. in surface voxels of
548 woodchip samples (Fig. 3) may reflect the fact that wood degradation is localized at surfaces that
549 are more readily exposed to DO and/or fungal biomass, and that Fe and Mn introduced into the
550 reactor as soil particles also accumulated at the wood surface, without a necessary mechanistic link
551 between metals and wood decay processes. We also cannot readily distinguish effects of Fe vs.
552 Mn, or potential synergies between Fe and Mn oxygenation reactions (e.g., H_2O_2 produced by Fe
553 redox reactions serving as the electron acceptor for MnP enzymes), on wood decay since Fe and
554 Mn co-occur on woodchip surfaces. Follow-up laboratory studies are underway to clarify
555 mechanisms linking redox reactions of Fe and/or Mn with wood degradation and denitrification
556 function. Biomolecular data on the presence and/or activity of white or brown rot fungi in the field
557 bioreactor samples would also have been helpful to differentiate between enzymatic (e.g.,

558 expression of MnP enzymes) and nonenzymatic (e.g., Fe-driven Fenton reaction) pathways for
559 wood degradation, both of which would be stimulated by exposure to DO.

560

561 **Environmental Implications.** We used a combination of bulk and micro-scale characterization
562 techniques to explore the biogeochemical factors regulating the degradation of lignocellulosic
563 wood material into bioavailable carbon for denitrifying microorganisms, an important bottleneck
564 that can limit the real-world effectiveness of woodchip bioreactors treating agricultural tile
565 drainage. Only woodchips in upstream portions of the bioreactor exhibited significant degradation,
566 and highly-degraded upstream woodchips released more carbon and supported faster NO_3^- removal
567 than less-degraded woodchips from midstream/downstream locations. This may be because even
568 the most highly-degraded woodchips retained an inner core replete with cellulose, and could thus
569 continue to serve as a source of bioavailable carbon. This insight into the micron-scale features of
570 wood biomass degradation was enabled by our novel application of synchrotron μX-ray scattering
571 techniques to visualize cellulose crystallinity in decomposing wood. Greater degradation of
572 upstream wood was most likely due to greater dissolved O_2 near the reactor influent which can
573 stimulate a host of enzymatic and nonenzymatic processes involved in lignocellulose decay.

574

575 These results highlight the need to enhance degradation of woodchips to increase their capacity
576 for NO_3^- removal. One practical approach to do this is to periodically drain reactors[88-89] to activate
577 O_2-dependent decomposition processes throughout the reactor and not just near the influent. Our
578 study highlights potential couplings between metal redox transformations and oxidative
579 depolymerization of complex biomolecules in the wood surface layer or the wood-water interface,
580 and suggests that effects of O_2 exposure on accelerating wood degradation into bioavailable carbon

may be enhanced in the presence of higher metal concentrations. Our results have implications for lignocellulosic biomass degradation in redox-dynamic environments beyond WBRs, including wetlands and sediment-water interfaces, and the multi-modal synchrotron-based techniques for visualizing cellulose degradation utilized here may have broad relevance for studies of lignocellulosic biomass degradation in the environment.

ASSOCIATED CONTENT

Supporting Information. Additional data and all experimental details are presented in Supporting Information section. This material is available free of charge via the Internet at http://pubs.acs.org.

AUTHOR INFORMATION

Corresponding Author: Matthew Reid

E-mail: mcr239@cornell.edu

Address: Civil and Environmental Engineering, Cornell University, Ithaca, NY 14853

Notes: The authors declare no competing financial interest.

Acknowledgements

This research was funded by NSF award 2237947. Parts of this research used the XFM and LiX Beamlines of the National Synchrotron Light Source II, a U.S. Department of Energy (DOE) Office of Science User Facility operated for the DOE Office of Science by Brookhaven National Laboratory under Contract No. DE-SC0012704. The LiX beamline is part of the Center for BioMolecular Structure (CBMS), which is primarily supported by the National Institutes of Health,

National Institute of General Medical Sciences (NIGMS) through a P30 Grant (P30GM133893), and by the DOE Office of Biological and Environmental Research (KP1605010). LiX also received additional support from NIH Grant S10 OD012331.

References

(1) Cecchetti, A. R.; Stiegler, A. N.; Gonthier, E. A.; Bandaru, S. R.; Fakra, S. C.; Alvarez-Cohen, L.; Sedlak, D. L., Fate of dissolved nitrogen in a horizontal levee: seasonal fluctuations in nitrate removal processes. *Environ Sci Technol* **2022,** *56* (4), 2770-2782.
(2) LeFevre, G. H.; Paus, K. H.; Natarajan, P.; Gulliver, J. S.; Novak, P. J.; Hozalski, R. M., Review of dissolved pollutants in urban storm water and their removal and fate in bioretention cells. *Journal of Environmental Engineering* **2015,** *141* (1), 04014050.
(3) Gorski, G.; Fisher, A. T.; Beganskas, S.; Weir, W. B.; Redford, K.; Schmidt, C.; Saltikov, C., Field and laboratory studies linking hydrologic, geochemical, and microbiological processes and enhanced denitrification during infiltration for managed recharge. *Environ Sci Technol* **2019,** *53* (16), 9491-9501.
(4) Halaburka, B. J.; LeFevre, G. H.; Luthy, R. G., Evaluation of Mechanistic Models for Nitrate Removal in Woodchip Bioreactors. *Environmental Science & Technology* **2017,** *51* (9), 5156-5164.
(5) Warneke, S.; Schipper, L. A.; Matiasek, M. G.; Scow, K. M.; Cameron, S.; Bruesewitz, D. A.; McDonald, I. R., Nitrate removal, communities of denitrifiers and adverse effects in different carbon substrates for use in denitrification beds. *Water research* **2011,** *45* (17), 5463-5475.
(6) Schipper, L. A.; Robertson, W. D.; Gold, A. J.; Jaynes, D. B.; Cameron, S. C., Denitrifying bioreactors—An approach for reducing nitrate loads to receiving waters. *Ecological engineering* **2010,** *36* (11), 1532-1543.
(7) Abusallout, I.; Hua, G., Characterization of dissolved organic carbon leached from a woodchip bioreactor. *Chemosphere* **2017,** *183*, 36-43.
(8) Zeikus, J.; Wellstein, A.; Kirk, T., Molecular basis for the biodegradative recalcitrance of lignin in anaerobic environments. *FEMS Microbiology Letters* **1982,** *15* (3), 193-197.
(9) Zeng, Y.; Zhao, S.; Yang, S.; Ding, S.-Y., Lignin plays a negative role in the biochemical process for producing lignocellulosic biofuels. *Current opinion in biotechnology* **2014,** *27*, 38-45.
(10) Schaefer, A.; Werning, K.; Hoover, N.; Tschirner, U.; Feyereisen, G.; Moorman, T. B.; Howe, A. C.; Soupir, M. L., Impact of flow on woodchip properties and subsidence in denitrifying bioreactors. *Agrosystems, Geosciences & Environment* **2021,** *4* (1), e20149.
(11) Ghane, E.; Feyereisen, G. W.; Rosen, C. J.; Tschirner, U. W., Carbon quality of four-year-old woodchips in a denitrification bed treating agricultural drainage water. *Transactions of the ASABE* **2018,** *61* (3), 995-1000.
(12) McGuire, P. M.; Butkevich, N.; Saksena, A. V.; Walter, M. T.; Shapleigh, J. P.; Reid, M. C., Oxic–anoxic cycling promotes coupling between complex carbon metabolism and denitrification in woodchip bioreactors. *Environ Microbiol* **2023,** *25* (9), 1696-1712.

(13) Wang, H.; Feyereisen, G. W.; Zhang, J.; Ishii, S., Fungal degradation of complex organic carbon supports denitrification in saturated woodchip bioreactors. *Bioresource Technology* **2025,** *417*, 131826.
(14) McGuire, P. M.; Dai, V.; Walter, M. T.; Reid, M. C., Labile carbon release from oxic–anoxic cycling in woodchip bioreactors enhances nitrate removal without increasing nitrous oxide accumulation. *Environmental Science: Water Research & Technology* **2021,** *7* (12), 2357-2371.
(15) Christianson, L. E.; Christianson, R. D.; Hay, C. H.; Seeman, A.; Díaz-García, C.; Feyereisen, G. W.; Pease, L.; Kjaersgaard, J.; Helmers, M. J.; Soupir, M., Denitrifying bioreactor surface subsidence varies with age and cover. *Ecological Engineering* **2025,** *211*, 107461.
(16) Christianson, L. E.; Feyereisen, G. W.; Hay, C.; Tschirner, U. W.; Kult, K.; Wickramarathne, N. M.; Hoover, N.; Soupir, M. L., Denitrifying bioreactor woodchip recharge: Media properties after nine years. *Transactions of the ASABE* **2020,** *63* (2), 407-416.
(17) Sanchez Bustamante-Bailon, A. P.; Margenot, A.; Cooke, R. A.; Christianson, L. E., Phosphorus removal in denitrifying woodchip bioreactors varies by wood type and water chemistry. *Environmental Science and Pollution Research* **2022,** *29* (5), 6733-6743.
(18) Li, H.; Santos, F.; Butler, K.; Herndon, E., A critical review on the multiple roles of manganese in stabilizing and destabilizing soil organic matter. *Environmental Science & Technology* **2021,** *55* (18), 12136-12152.
(19) Kleber, M.; Eusterhues, K.; Keiluweit, M.; Mikutta, C.; Mikutta, R.; Nico, P. S., Mineral–organic associations: formation, properties, and relevance in soil environments. *Advances in agronomy* **2015,** *130*, 1-140.
(20) Wagai, R.; Mayer, L. M., Sorptive stabilization of organic matter in soils by hydrous iron oxides. *Geochim. Cosmochim. Acta* **2007,** *71* (1), 25-35.
(21) Chen, C.; Dynes, J. J.; Wang, J.; Sparks, D. L., Properties of Fe-organic matter associations via coprecipitation versus adsorption. *Environ Sci Technol* **2014,** *48* (23), 13751-13759.
(22) Riedel, T.; Zak, D.; Biester, H.; Dittmar, T., Iron traps terrestrially derived dissolved organic matter at redox interfaces. *Proceedings of the National Academy of Sciences* **2013,** *110* (25), 10101-10105.
(23) Mikutta, R.; Kleber, M.; Torn, M. S.; Jahn, R., Stabilization of soil organic matter: association with minerals or chemical recalcitrance? *Biogeochemistry* **2006,** *77*, 25-56.
(24) Barber, A.; Brandes, J.; Leri, A.; Lalonde, K.; Balind, K.; Wirick, S.; Wang, J.; Gélinas, Y., Preservation of organic matter in marine sediments by inner-sphere interactions with reactive iron. *Scientific Reports* **2017,** *7* (1), 366.
(25) Kleber, M.; Bourg, I. C.; Coward, E. K.; Hansel, C. M.; Myneni, S. C.; Nunan, N., Dynamic interactions at the mineral–organic matter interface. *Nature Reviews Earth & Environment* **2021,** *2* (6), 402-421.
(26) Hofrichter, M., lignin conversion by manganese peroxidase (MnP). *Enzyme and Microbial technology* **2002,** *30* (4), 454-466.
(27) Jones, M. E.; LaCroix, R. E.; Zeigler, J.; Ying, S. C.; Nico, P. S.; Keiluweit, M., Enzymes, Manganese, or Iron? Drivers of Oxidative Organic Matter Decomposition in Soils. *Environmental Science & Technology* **2020,** *54* (21), 14114-14123.
(28) Hall, S. J.; Silver, W. L., Iron oxidation stimulates organic matter decomposition in humid tropical forest soils. *Global change biology* **2013,** *19* (9), 2804-2813.

(29) Trusiak, A.; Treibergs, L. A.; Kling, G. W.; Cory, R. M., The role of iron and reactive oxygen species in the production of CO2 in arctic soil waters. *Geochimica et Cosmochimica Acta* **2018,** *224*, 80-95.
(30) Cragg, S. M.; Beckham, G. T.; Bruce, N. C.; Bugg, T. D.; Distel, D. L.; Dupree, P.; Etxabe, A. G.; Goodell, B. S.; Jellison, J.; McGeehan, J. E., Lignocellulose degradation mechanisms across the Tree of Life. *Current opinion in chemical biology* **2015,** *29*, 108-119.
(31) Wood, P. M., Pathways for production of Fenton's reagent by wood-rotting fungi. *FEMS Microbiology Reviews* **1994,** *13* (2-3), 313-320.
(32) Chen, C.; Hall, S. J.; Coward, E.; Thompson, A., Iron-mediated organic matter decomposition in humid soils can counteract protection. *Nature communications* **2020,** *11* (1), 1-13.
(33) Houghton, R.; Hall, F.; Goetz, S. J., Importance of biomass in the global carbon cycle. *Journal of Geophysical Research: Biogeosciences* **2009,** *114* (G2).
(34) Keiluweit, M.; Nico, P.; Harmon, M. E.; Mao, J.; Pett-Ridge, J.; Kleber, M., Long-term litter decomposition controlled by manganese redox cycling. *Proceedings of the National Academy of Sciences* **2015,** *112* (38), E5253-E5260.
(35) Sun, T.; Cui, Y.; Berg, B.; Zhang, Q.; Dong, L.; Wu, Z.; Zhang, L., A test of manganese effects on decomposition in forest and cropland sites. *Soil Biology and Biochemistry* **2019,** *129*, 178-183.
(36) Feyereisen, G. W.; Ghane, E.; Schumacher, T. W.; Dalzell, B. J.; Williams, M. R., Can woodchip bioreactors be used at a catchment scale? Nitrate performance and sediment considerations. *Journal of the ASABE* **2023,** *66* (2), 367-379.
(37) Howell, C.; Hastrup, A. C. S.; Goodell, B.; Jellison, J., Temporal changes in wood crystalline cellulose during degradation by brown rot fungi. *International Biodeterioration & Biodegradation* **2009,** *63* (4), 414-419.
(38) Hassanpour, B.; Giri, S.; Pluer, W. T.; Steenhuis, T. S.; Geohring, L. D., Seasonal performance of denitrifying bioreactors in the Northeastern United States: Field trials. *Journal of Environmental Management* **2017,** *202*, 242-253.
(39) Pluer, W. T.; Geohring, L. D.; Steenhuis, T. S.; Walter, M. T., Controls influencing the treatment of excess agricultural nitrate with denitrifying bioreactors. *Journal of Environmental Quality* **2016,** *45* (3), 772-778.
(40) Pluer, W. T.; Morris, C. K.; Walter, M. T.; Geohring, L. D., Denitrifying bioreactor response during storm events. *Agricultural Water Management* **2019,** *213*, 1109-1115.
(41) Zhang, Z.; Echavarria, S.; Sang, Y.; Weidman, G. R.; Napp, N.; Reid, M. C., Real-Time Control of Exogenous Carbon Dosing in a Denitrifying Woodchip Bioreactor Treating Agricultural Drainage. *ACS ES&T Engineering* **2024,** *4* (6), 1433-1443.
(42) Patzner MS, M. C., Malusova M, Baur M, Nikeleit V, Scholten T, Hoeschen C, Byrne JM, Borch T, Kappler A, Bryce C., Iron mineral dissolution releases iron and associated organic carbon during permafrost thaw. *Nat Commun* **2020,** *11* (1), 6329.
(43) Jansen, B.; Tonneijck, F.; Verstraten, J., Selective extraction methods for aluminium, iron and organic carbon from montane volcanic ash soils. *Pedosphere* **2011,** *21* (5), 549-565.
(44) Weishaar, J. L.; Aiken, G. R.; Bergamaschi, B. A.; Fram, M. S.; Fujii, R.; Mopper, K., Evaluation of specific ultraviolet absorbance as an indicator of the chemical composition and reactivity of dissolved organic carbon. *Environmental science & technology* **2003,** *37* (20), 4702-4708.

(45) Bach, C. E.; Warnock, D. D.; Van Horn, D. J.; Weintraub, M. N.; Sinsabaugh, R. L.; Allison, S. D.; German, D. P., Measuring phenol oxidase and peroxidase activities with pyrogallol, L-DOPA, and ABTS: effect of assay conditions and soil type. *Soil Biology and Biochemistry* **2013,** *67*, 183-191.
(46) Hendel, B.; Sinsabaugh, R. L.; Marxsen, J., Lignin-degrading enzymes: phenoloxidase and peroxidase. *Methods to study litter decomposition: a practical guide* **2020**, 425-431.
(47) Sinsabaugh, R. L.; Gallo, M. E.; Lauber, C.; Waldrop, M. P.; Zak, D. R., Extracellular enzyme activities and soil organic matter dynamics for northern hardwood forests receiving simulated nitrogen deposition. *Biogeochemistry* **2005,** *75*, 201-215.
(48) Sinsabaugh, R. L., Phenol oxidase, peroxidase and organic matter dynamics of soil. *Soil Biology and Biochemistry* **2010,** *42* (3), 391-404.
(49) Hug, S. J.; Leupin, O., Iron-catalyzed oxidation of arsenic (III) by oxygen and by hydrogen peroxide: pH-dependent formation of oxidants in the Fenton reaction. *Environmental science & technology* **2003,** *37* (12), 2734-2742.
(50) Remucal, C. K.; Sedlak, D. L., The role of iron coordination in the production of reactive oxidants from ferrous iron oxidation by oxygen and hydrogen peroxide. In *Aquatic redox chemistry*, ACS Publications: 2011; pp 177-197.
(51) Fang, L.; Wang, Y.; Sardar, M. F.; Tang, C.; Fang, T.; Du, J.; Yan, E.; Zhang, Q.; Li, Y., Soil fungal composition under decomposing deadwood is largely affected by tree bark density rather than soil properties. *Applied Soil Ecology* **2024,** *198*, 105373.
(52) Goldin, S. R.; Hutchinson, M. F., Coarse woody debris modifies surface soils of degraded temperate eucalypt woodlands. *Plant Soil* **2013,** *370*, 461-469.
(53) Zalamea, M.; González, G.; Lodge, D. J., Physical, chemical, and biological properties of soil under decaying wood in a tropical wet forest in Puerto Rico. *Forests* **2016,** *7* (8), 168.
(54) Nichols, R. S.; Martin, P., Low biodegradability of dissolved organic matter from Southeast Asian peat‐draining rivers. *Journal of Geophysical Research: Biogeosciences* **2021,** *126* (6), e2020JG006182.
(55) Yang, L.; Liu, J.; Chodankar, S.; Antonelli, S.; DiFabio, J., Scanning structural mapping at the Life Science X-ray Scattering Beamline. *Journal of Synchrotron Radiation* **2022,** *29* (2), 540-548.
(56) Yang, L., X-ray scattering based scanning tomography for imaging and structural characterization of cellulose in plants. *Synchrotron Radiation* **2024,** *31* (4), 936-947.
(57) Barbour, A.; Cai, Y. Q.; Fluerasu, A.; Freychet, G.; Fukuto, M.; Gang, O.; Gann, E.; Laasch, R.; Li, R.; Ocko, B. M., X-ray scattering for soft matter research at NSLS-II. *Synchrotron radiation news* **2023,** *36* (2), 24-30.
(58) Lionetto, F.; Del Sole, R.; Cannoletta, D.; Vasapollo, G.; Maffezzoli, A., Monitoring wood degradation during weathering by cellulose crystallinity. *Materials* **2012,** *5* (10), 1910-1922.
(59) Park, S.; Baker, J. O.; Himmel, M. E.; Parilla, P. A.; Johnson, D. K., Cellulose crystallinity index: measurement techniques and their impact on interpreting cellulase performance. *Biotechnology for biofuels* **2010,** *3*, 1-10.
(60) Hastrup, A. C. S.; Howell, C.; Larsen, F. H.; Sathitsuksanoh, N.; Goodell, B.; Jellison, J., Differences in crystalline cellulose modification due to degradation by brown and white rot fungi. *Fungal biology* **2012,** *116* (10), 1052-1063.
(61) Ge, M.; Huang, X.; Yan, H.; Gursoy, D.; Meng, Y.; Zhang, J.; Ghose, S.; Chiu, W. K.; Brinkman, K. S.; Chu, Y. S., Three-dimensional imaging of grain boundaries via quantitative fluorescence X-ray tomography analysis. *Communications Materials* **2022,** *3* (1), 37.

(62) Zelinka, S. L.; Jakes, J. E.; Kirker, G. T.; Bishell, A. B.; Boardman, C. R.; Lai, B.; Sterbinsky, G. E.; Jellison, J.; Goodell, B., Oxidation states of iron and manganese in lignocellulose altered by the brown rot fungus Gloeophyllum trabeum measured in-situ using X-ray absorption near edge spectroscopy (XANES). *International Biodeterioration & Biodegradation* **2021,** *158*, 105162.
(63) Wilke, M.; Farges, F.; Petit, P.-E.; Brown Jr, G. E.; Martin, F., Oxidation state and coordination of Fe in minerals: An Fe K-XANES spectroscopic study. *Am Mineral* **2001,** *86* (5-6), 714-730.
(64) Zahoransky, T.; V. Wegorzewski, A.; Huong, W.; Mikutta, C., X-ray absorption spectroscopy study of Mn reference compounds for Mn speciation in terrestrial surface environments. *American Mineralogist* **2023,** *108* (5), 847-864.
(65) Feyereisen, G. W.; Wang, H.; Wang, P.; Anderson, E. L.; Jang, J.; Ghane, E.; Coulter, J. A.; Rosen, C. J.; Sadowsky, M. J.; Ishii, S., Carbon supplementation and bioaugmentation to improve denitrifying woodchip bioreactor performance under cold conditions. *Ecological Engineering* **2023,** *191*, 106920.
(66) Anderson, C. G.; Tfaily, M. M.; Chu, R. K.; Tolić, N.; Fox, P. M.; Nico, P. S.; Fendorf, S.; Keiluweit, M., Seasonal Controls on Microbial Depolymerization and Oxidation of Organic Matter in Floodplain Soils. *Environ Sci Technol* **2024,** *58* (38), 16815-16823.
(67) Kirker, G.; Zelinka, S.; Gleber, S.-C.; Vine, D.; Finney, L.; Chen, S.; Hong, Y. P.; Uyarte, O.; Vogt, S.; Jellison, J., Synchrotron-based X-ray fluorescence microscopy enables multiscale spatial visualization of ions involved in fungal lignocellulose deconstruction. *Scientific reports* **2017,** *7* (1), 1-15.
(68) Kirker, G.; Zelinka, S.; Gleber, S.-C.; Vine, D.; Finney, L.; Chen, S.; Hong, Y. P.; Uyarte, O.; Vogt, S.; Jellison, J., Synchrotron-based X-ray fluorescence microscopy enables multiscale spatial visualization of ions involved in fungal lignocellulose deconstruction. *Scientific reports* **2017,** *7* (1), 41798.
(69) Duggan DiDominic, K. L.; Shapleigh, J. P.; Walter, M. T.; Wang, Y. S.; Reid, M. C.; Regan, J. M. *Microbial diversity and gene abundance in denitrifying bioreactors: A comparison of the woodchip surface biofilm versus the interior wood matrix*; 0047-2425; Wiley Online Library: 2024.
(70) Borch, T.; Kretzschmar, R.; Kappler, A.; Cappellen, P. V.; Ginder-Vogel, M.; Voegelin, A.; Campbell, K., Biogeochemical redox processes and their impact on contaminant dynamics. *Environmental science & technology* **2010,** *44* (1), 15-23.
(71) Liang, G., *Iron uptake, signaling, and sensing in plants*. 2022; Vol. 3.
(72) Morrissey, J.; Guerinot, M. L., Iron uptake and transport in plants: the good, the bad, and the ionome. *Chem Rev* **2009,** *109* (10), 4553-4567.
(73) Alejandro, S.; Höller, S.; Meier, B.; Peiter, E., Manganese in plants: from acquisition to subcellular allocation. *Frontiers in plant science* **2020,** *11*, 300.
(74) Herndon, E. M.; Martínez, C. E.; Brantley, S. L., Spectroscopic (XANES/XRF) characterization of contaminant manganese cycling in a temperate watershed. *Biogeochemistry* **2014,** *121*, 505-517.
(75) Aldossari, N.; Ishii, S., Isolation of cold‐adapted nitrate‐reducing fungi that have potential to increase nitrate removal in woodchip bioreactors. *Journal of Applied Microbiology* **2021,** *131* (1), 197-207.

(76) Jéglot, A.; Audet, J.; Sørensen, S. R.; Schnorr, K.; Plauborg, F.; Elsgaard, L., Microbiome structure and function in woodchip bioreactors for nitrate removal in agricultural drainage water. *Frontiers in microbiology* **2021,** *12*, 678448.
(77) Bonnarme, P.; Jeffries, T. W., Mn (II) regulation of lignin peroxidases and manganese-dependent peroxidases from lignin-degrading white rot fungi. *Applied and Environmental Microbiology* **1990,** *56* (1), 210-217.
(78) Kanaparthi, D.; Pommerenke, B.; Casper, P.; Dumont, M. G., Chemolithotrophic nitrate-dependent Fe (II)-oxidizing nature of actinobacterial subdivision lineage TM3. *The ISME journal* **2013,** *7* (8), 1582-1594.
(79) Liu, T.; Chen, D.; Luo, X.; Li, X.; Li, F., Microbially mediated nitrate-reducing Fe (II) oxidation: quantification of chemodenitrification and biological reactions. *Geochim. Cosmochim. Acta* **2019,** *256*, 97-115.
(80) Carlson, H. K.; Clark, I. C.; Blazewicz, S. J.; Iavarone, A. T.; Coates, J. D., Fe (II) oxidation is an innate capability of nitrate-reducing bacteria that involves abiotic and biotic reactions. *Journal of bacteriology* **2013,** *195* (14), 3260-3268.
(81) Dong, H.; Zeng, Q.; Sheng, Y.; Chen, C.; Yu, G.; Kappler, A., Coupled iron cycling and organic matter transformation across redox interfaces. *Nature Reviews Earth & Environment* **2023,** *4* (9), 659-673.
(82) Chen, C.; Hall, S. J.; Coward, E.; Thompson, A., Iron-mediated organic matter decomposition in humid soils can counteract protection. *Nat Commun* **2020,** *11* (1), 2255.
(83) Page, S. E.; Kling, G. W.; Sander, M.; Harrold, K. H.; Logan, J. R.; McNeill, K.; Cory, R. M., Dark formation of hydroxyl radical in arctic soil and surface waters. *Environmental science & technology* **2013,** *47* (22), 12860-12867.
(84) Hammel, K. E.; Kapich, A. N.; Jensen Jr, K. A.; Ryan, Z. C., Reactive oxygen species as agents of wood decay by fungi. *Enzyme and microbial technology* **2002,** *30* (4), 445-453.
(85) Tamaru, Y.; Yoshida, M.; Eltis, L. D.; Goodell, B., Multiple iron reduction by methoxylated phenolic lignin structures and the generation of reactive oxygen species by lignocellulose surfaces. *International journal of biological macromolecules* **2019,** *128*, 340-346.
(86) Arantes, V.; Milagres, A. M.; Filley, T. R.; Goodell, B., Lignocellulosic polysaccharides and lignin degradation by wood decay fungi: the relevance of nonenzymatic Fenton-based reactions. *Journal of Industrial Microbiology and Biotechnology* **2011,** *38* (4), 541-555.
(87) Liu, X.; Ding, S.; Gao, F.; Wang, Y.; Taherzadeh, M. J.; Wang, Y.; Qin, X.; Wang, X.; Luo, H.; Yao, B., Exploring the cellulolytic and hemicellulolytic activities of manganese peroxidase for lignocellulose deconstruction. *Biotechnology for Biofuels and Bioproducts* **2023,** *16* (1), 139.
(88) Maxwell, B. M.; Birgand, F.; Schipper, L. A.; Christianson, L. E.; Tian, S.; Helmers, M. J.; Williams, D. J.; Chescheir, G. M.; Youssef, M. A., Drying–rewetting cycles affect nitrate removal rates in woodchip bioreactors. *Journal of environmental quality* **2019,** *48* (1), 93-101.
(89) Maxwell, B. M.; Birgand, F.; Schipper, L. A.; Christianson, L. E.; Tian, S.; Helmers, M. J.; Williams, D. J.; Chescheir, G. M.; Youssef, M. A., Increased Duration of Drying–Rewetting Cycles Increases Nitrate Removal in Woodchip Bioreactors. *Agricultural & Environmental Letters* **2019,** *4* (1), 190028.

868

869

870

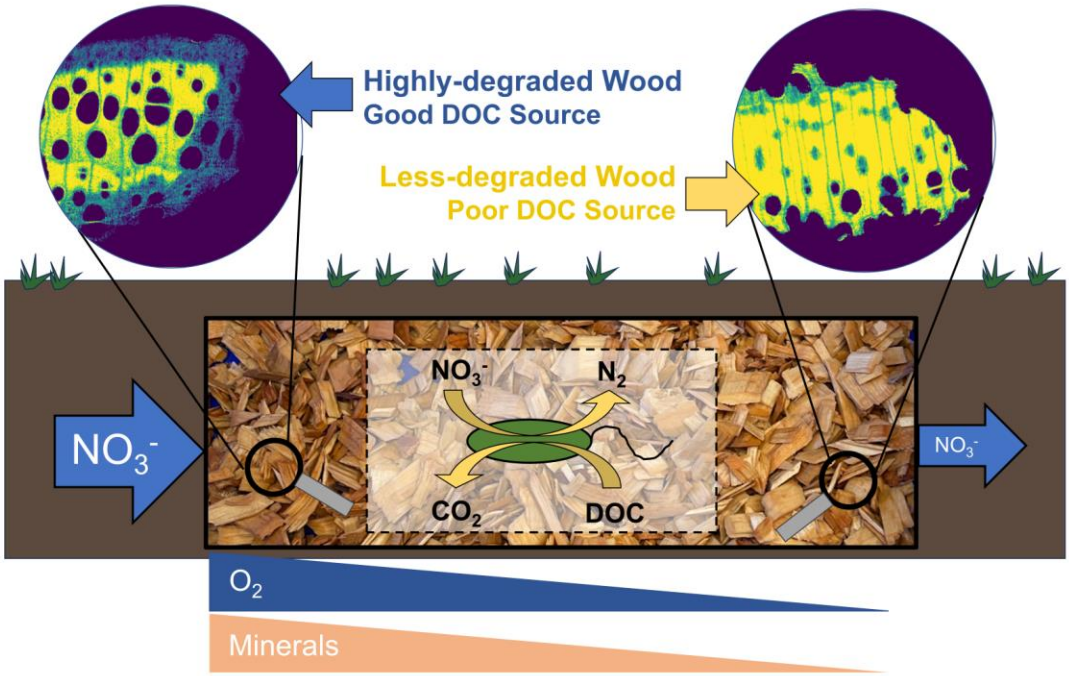

871

872 TOC Figure